Global climate modeling of Saturn's atmosphere. Part I: Evaluation of the radiative transfer model

S. Guerlet [a,b,*], A. Spiga [a,b], M. Sylvestre [a,b,d], M. Indurain [a,b], T. Fouchet [c,d], J. Leconte [f,a,b], E. Millour [a,b], R. Wordsworth [e], M. Capderou [a,b], B. Bézard [d], F. Forget [a,b]

[a] Sorbonne Universités, UPMC Paris 06, UMR 8539, LMD, F-75005 Paris, France
[b] CNRS, LMD, IPSL, UMR 8539, 4 Place Jussieu, F-75005 Paris, France
[c] Sorbonne Universités, UPMC Paris 06, UMR 8109, LESIA, F-75005 Paris, France
[d] LESIA, Observatoire de Paris, CNRS, UPMC, Université Paris-Diderot, 5 place Jules Janssen, 92195 Meudon, France
[e] University of Chicago, Department of Geological Sciences, 60622 Chicago, USA
[f] Canadian Institute for Theoretical Astrophysics, 60 St. George St., Toronto M5S 3H8, Canada

ARTICLE INFO

ABSTRACT

We have developed and optimized a seasonal, radiative–convective model of Saturn's upper troposphere and stratosphere. It is used to investigate Saturn's radiatively-forced thermal structure between 3 and 10^{-6} bar, and is intended to be included in a Saturn global climate model (GCM), currently under development. The main elements of the radiative transfer model are detailed as well as the sensitivity to spectroscopic parameters, hydrocarbon abundances, aerosol properties, oblateness, and ring shadowing effects. The vertical temperature structure and meridional seasonal contrasts obtained by the model are then compared to Cassini/CIRS observations. Several significant model-observation mismatches reveal that Saturn's atmosphere departs from radiative equilibrium. For instance, we find that the modeled temperature profile is close to isothermal above the 2-mbar level, while the temperature retrieved from ground-based or Cassini/CIRS data continues to increase with altitude. Also, no local temperature minimum associated to the ring shadowing is observed in the data, while the model predicts stratospheric temperatures 10 K to 20 K cooler than in the absence of rings at winter tropical latitudes. These anomalies are strong evidence that processes other that radiative heating and cooling control Saturn's stratospheric thermal structure. Finally, the model is used to study the warm stratospheric anomaly triggered after the 2010 Great White Spot. Comparison with recent Cassini/CIRS observations suggests that the rapid cooling phase of this warm "beacon" in May–June 2011 can be explained by radiative processes alone. Observations on a longer timeline are needed to better characterize and understand its long-term evolution.

© 2014 Elsevier Inc. All rights reserved.

1. Introduction

Saturn's upper tropospheric and stratospheric thermal structure is governed by radiative and dynamical processes, both controlled by seasonal variations in insolation over the course of Saturn's 29.5 year orbit. Radiative cooling occurs primarily through thermal emission of hydrocarbons (mainly methane, ethane and acetylene) along with collision-induced absorption (CIA) by H_2–H_2 and H_2–He in the thermal infrared. Radiative heating mainly results from absorption of visible and near-infrared solar photons by methane and aerosols. Seasonal and orbital variations in insolation have a

direct effect on the net heating rates, through variations in solar energy deposition, as well as an indirect effect due to the modulation of photochemical activity, impacting hydrocarbon and aerosol abundances (and hence the associated radiative cooling/heating rates). Furthermore, aerosols and hydrocarbons can be transported by Saturn's large-scale circulation, which in turn impacts the radiative budget and the temperature fields.

Over the last decade, ground-based and space-based spectroscopic infrared mapping of Saturn's atmospheric thermal structure and composition have been obtained with unprecedent details. In particular, the Composite Infrared Spectrometer (CIRS) instrument onboard Cassini has been acquiring data for 8 years (2004–2013), long enough to monitor seasonal variations in temperature and composition (Fletcher et al., 2010; Sinclair et al., 2013).

* Corresponding author at: CNRS, LMD, IPSL, UMR 8539, 4 Place Jussieu, F-75005, Paris, France.
E-mail address: sandrine.guerlet@lmd.jussieu.fr (S. Guerlet).

These observations reveal that Saturn's lower stratosphere exhibit large temperature contrasts with latitude and season. For instance, in 2005 (solar longitude $L_S = 300°$), a pole-to-pole temperature contrast of 40 K was measured at the 1-mbar level between the southern (summer) and northern (winter) hemispheres (Fletcher et al., 2007). Following the 2009 equinox, high southern latitudes have cooled down by 10–15 K as they were entering autumnal darkness, while northern mid-latitudes have warmed by 6–10 K as they emerged from ring-shadow to spring-time conditions (Fletcher et al., 2010; Sinclair et al., 2013). In contrast, tropospheric temperatures exhibit moderate hemispherical asymmetries (10 K at 100 mbar at $L_S = 300°$) and seasonal variations (only 2–3 K over 4 years), consistent with the longer radiative time constants at higher pressures.

On top of these overall seasonal trends, the observed temperature fields display several anomalies, which are thought to be of dynamical origin. The temperature in the equatorial region features a remarkable periodic oscillation characterized by the superposition of warm and cold regions, associated with a strong vertical wind shear of 200 m/s (Fouchet et al., 2008; Orton et al., 2008; Guerlet et al., 2011; Schinder et al., 2011). This pattern is reminiscent of analogous periodic oscillations in the Earth's stratosphere (the Quasi-Biennial Oscillation and the Semi-Annual Oscillation), which are governed by interactions between vertically-propagating waves and the mean zonal flow (Baldwin et al., 2001). Other thermal anomalies on Saturn include the observation of polar hot spots at both poles, supposedly linked to the polar vortices (Fletcher et al., 2008), and the occurrence of a spectacular stratospheric warming at 40°N (called "beacon") following Saturn's tropospheric Great White Storm in December 2010, still visible in 2012 (Fletcher et al., 2012).

Global climate modeling of Saturn's atmosphere is needed in order to better interpret the observed temperature fields, their seasonal variations, and disentangle the effects of radiative and dynamical processes. In the 1980s, following Voyager fly-bys, several 2D radiative–convective models have been developed, including or not seasonal effects (Appleby and Hogan, 1984; Bézard et al., 1984; Bézard and Gautier, 1985). Since then, major updates in the knowledge of hydrocarbon abundances (in particular obtained from Cassini observations), and their spectroscopic properties, have motivated a revision of these early models. For instance, Greathouse et al. (2008) have developed a seasonal radiative transfer model of Saturn's stratosphere and used it to interpret Cassini/CIRS observations in the 5–0.5 mbar pressure range (Fletcher et al., 2010).

Our aim is twofold: first, to build an up-to-date and versatile radiative–convective climate model of Saturn's upper troposphere and stratosphere that allows for comparison with temperature profiles measured in the full range of Cassini/CIRS vertical sensitivity (500–0.01 mbar). Secondly, to make this seasonal model fitted for implementation in a dynamical global climate model (GCM) of Saturn's atmosphere, with the aim of better understanding Saturn's stratospheric circulation, still poorly known.

Several numerical challenges arise when developing a Saturn GCM: on the one hand, a 3D numerical grid of high spatial resolution is needed to resolve dynamical processes (at least 512×384 elements in longitude $\times$ latitude, as constrained by Saturn's Rossby deformation radius); on the other hand, the long timescales of the seasonal radiative forcing compared to the short timescales of some atmospheric motions imply running simulations for several Saturn years, with calculations of radiative forcings every few Saturn days. Hence, there is a need for developing a fast and robust radiative transfer model for Saturn's atmosphere, in order to accurately compute atmospheric heating and cooling rates on each grid point of a GCM. Modeling efforts in this field are very recent, as most existing giant planet's dynamical models focus on the

tropospheric layer (Morales-Juberias et al., 2003; Liu and Schneider, 2010; Lian and Showman, 2010), where radiative processes represent a minor contribution in the energy balance. Recently, Friedson and Moses (2012) presented results from a 3D GCM of Saturn's upper troposphere and stratosphere, which included a full radiative transfer scheme (using k-distributions). While the authors focused on deriving the effective advective circulation and eddy transport coefficients, specific aspects pertaining to the optimization and validation of the radiative transfer were not covered.

Here we report on the development and optimization of a radiative–convective model that uses up-to-date, state-of-the-art gaseous and aerosol opacities. This model can be used independently to study Saturn's radiatively-forced thermal structure, while it also meets the accuracy and computational efficiency required for an implementation in a Saturn 3D GCM, which will be detailed in a future manuscript. The main elements of the radiative transfer model are reviewed in Section 2, along with several sensitivity studies to, for instance, spectroscopic parameters and aerosol scenarios. In Section 3, the vertical and seasonal thermal contrasts obtained by the radiative–convective model are described, and the impact of ring shadowing and aerosols on the upper tropospheric and stratospheric temperature are evaluated. In Section 4, these results are discussed and compared to Cassini/CIRS observations. Finally, this model is applied to the study of the warm stratospheric anomaly triggered after the 2010 storm in Section 5, before concluding in Section 6.

2. A radiative–convective model of Saturn's atmosphere

2.1. Overall description

The radiative–convective model employed in this study is derived from existing tools developed as part as a generic version of the Laboratoire de Météorologie Dynamique (LMD) global climate model (GCM), used to simulate the radiative forcing and large-scale circulation of terrestrial exoplanets (Wordsworth et al., 2011; Leconte et al., 2013a,b) and primitive atmospheres (Charnay et al., 2013; Forget et al., 2013; Wordsworth et al., 2010a). The radiative part uses a two-stream approximation to solve the radiative transfer equations including multiple scattering as proposed by Toon et al. (1989). Rayleigh scattering is included following the method described in Hansen and Travis (1974). As line-by-line calculations are too time-consuming for GCM applications, a k-distribution model (described in Section 2.2) is used to compute gaseous opacities (Goody and Yung, 1989; Wordsworth et al., 2010b). Tests are performed to assess the importance of the diurnal cycle, which is found negligible. Rather, given Saturn's long radiative timescales, a daily-averaged solar flux is considered and calculations of the radiative heating and cooling rates are performed typically once every 10 (Saturn) days.

In this study, focused on the radiatively-forced thermal structure, computations in the dynamical part of the LMD GCM are not performed. A convective adjustment scheme relaxes the temperature profile towards the adiabatic lapse rate (g/C_p, with g the gravity and C_p the specific heat capacity) when an unstable temperature lapse rate is encountered after the radiative calculations (Hourdin et al., 1993).

The above-mentioned generic model is adapted to match Saturn's atmospheric conditions (composition, temperature and pressure) and external forcings. The nominal model includes opacities due to CH_4, C_2H_6, C_2H_2, collision-induced absorption by $H_2–H_2$, $H_2–He$ and two aerosol layers. Hydrogen and helium fractions are set to, respectively, 0.86 and 0.1355 consistently with an analysis of Voyager measurements by Conrath and

Gautier (2000). Methane volume mixing ratio is set to 4.5×10^{-3} below the 1 bar pressure level (Flasar et al., 2005) and decreases with height to account for photochemistry and vertical mixing, following Moses et al. (2000). C_2H_6 and C_2H_2 abundance vertical profiles correspond to the mean of the profiles retrieved from Cassini/CIRS observations by Guerlet et al. (2009) between 40°N and 40°S (planetocentric). Hereafter, all quoted latitudes are planetocentric.

The atmospheric model pressure grid consists of 64 pressure levels between 3 and 10^{-6} bars. An internal heat flux independent of latitude is added in order to match Saturn's total emitted power of 4.9 W m^{-2} (Li et al., 2010), as justified in Section 2.5. To compute the heat capacity, one would need to take into account the temperature dependency of the H_2 heat capacity, along with the dependency on the ortho/para ratio. However, these dependences are not well constrained and also depend on vertical motions. We thus choose to set the H_2 heat capacity to its value at 1 bar (130 K), where the ortho/para hydrogen ratio is close to its high-temperature equilibrium value of 3:1. This approximation does not impact significantly the results above the radiative–convective boundary, which is our region of interest. Heat capacity for the H_2/He mixture is hence fixed to 11,500 J kg^{-1} K^{-1}.

We set the solar longitude of Saturn's perihelion to 280.08°, a value obtained from calculations based on J2000 parameters. Saturn's obliquity is set to 26.73°, and its eccentricity to 0.055. Ring shadowing effects, considering different opacities for the A, B and C rings, and the Cassini division, are included in the computation of the diurnal-averaged insolation using a formalism described in Appendix A. Finally, Saturn's oblate shape is taken into account in two ways: in the calculation of the incident solar flux, and in the computation of a latitude-dependent gravity field (see Supplementary Material).

2.2. Construction of the k-distribution model

The *k*-distribution model of gaseous opacities is built in several steps. Firstly, absorption coefficient (k_v) spectra are calculated in the range 10–25,000 cm^{-1} (0.4 µm – 1 mm) for a mixture of gases (CH_4, C_2H_6, C_2H_2) using kspectrum, a line-by-line model developed by Vincent Eymet, available online at http://code.google.com/p/kspectrum/. Spectroscopic parameters are extracted from the HITRAN 2012 database (Rothman et al., 2013). A Voigt lineshape model is used, where air-broadened coefficients are replaced with H_2-broadened coefficients when available: for CH_4 we use a pressure-broadening coefficient of 0.065 cm^{-1} atm^{-1} with a T^{-n} temperature dependence of $n = 0.44$, while for C_2H_6 n is set to 0.94 (Halsey et al., 1988; Margolis, 1993). High-resolution spectra are computed on a 2-D parameter grid comprising twelve different temperatures (70–400 K) times eight pressure levels (10–10^{-6} bar) to cover the range of Saturn's atmospheric conditions. Examples of absorption coefficient spectra at $p = 1$ mbar and $T = 160$ K are shown in Figs. 1 and 2 for the visible/near-infrared and thermal infrared part, respectively. In a second step, these spectra are divided into several spectral bands (how these band limits are chosen is detailed in Section 2.3.2). For each (p, T) condition, correlated-k coefficients are generated by sorting the high-resolution spectrum in each band according to the strength of the discrete absorption coefficients k_v, in a cumulated distribution space $g(k)$. The end product is the function $k(g)$, which is much smoother than k_v and can be approximated by a limited number of weighted points. Subsequently, instead of integrating the radiative transfer equations in the frequency space v (where absorption spectra are highly variable), integration is done over only 16 points in g-space, whose abscissa (g_i) and weights (Δg_i) are given in Table 1.
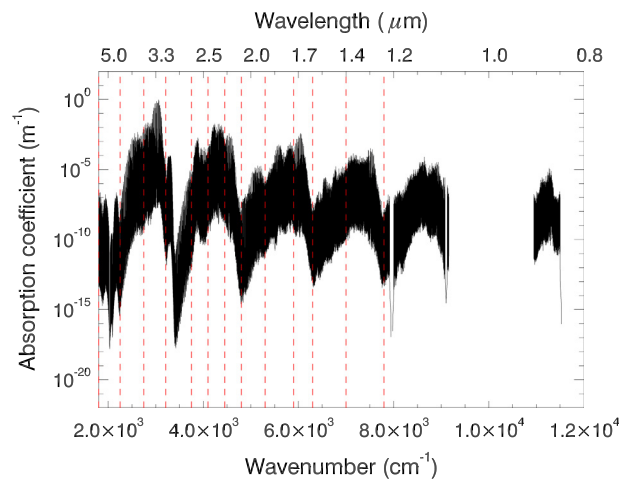

Fig. 1. Absorption coefficient spectrum calculated for a pressure of 1 mbar and a temperature of 160 K in the visible range from the HITRAN 2012 database. The vertical dashed lines represent the limits of the 12 bands used in the constructed *k*-distribution model.
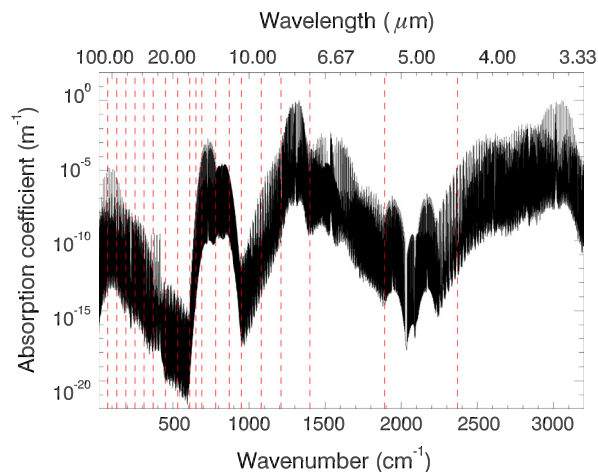

Fig. 2. Same as Fig. 1 for the infrared part of the spectrum.

Table 1
Abscissa (g_i) and weights (Δg_i) in g-space used for generating the *k*-distribution coefficients.

g_i	Δg_i
0.04068415	0.08136831
0.14206561	0.12139460
0.26997545	0.13442509
0.40263812	0.13090025
0.52717084	0.11816520
0.63684743	0.10118797
0.72902450	0.08316617
0.80361755	0.06601992
0.86201713	0.050779238
0.90634632	0.037879155
0.93897476	0.027377720
0.96221959	0.019111938
0.97817822	0.012805328
0.98865035	0.008138922
0.99511755	0.004795479
0.99875764	0.002484713

2.3. Sensitivity studies and optimization of the k-distribution model

In order to test and optimize our *k*-distribution model, several aspects of the construction of the *k*-distribution coefficients are

investigated: the discretization in pressure space and the spectral band discretization. Furthermore, the impact of adopting recent updates in methane spectroscopy (in the HITRAN database or from empirical band models) is explored. In the following, the sensitivity of the vertical profiles of temperature and heating rate to these different parameterizations is assessed using 1-D radiative–convective runs.

2.3.1. Sensitivity to the choice of pressure levels

The k-distribution coefficients are computed separately only once, on a reference pressure grid, and are then interpolated to the pressure levels corresponding to the radiative transfer model grid. As the shape of the individual absorption lines varies strongly with pressure, potential errors introduced by this interpolation need to be assessed. To do this, a first set of k-distribution coefficients is generated every pressure decade (8 levels), and another set every 0.5 in $\log(p)$ (15 levels). The effect of using twice as much reference pressure levels on the heating rates is found to be negligible in our case: at most, a change of 0.4% is obtained when 15 reference pressure levels are used instead of 8, which corresponds to an error less than 0.4 K on the temperature profile. The use of 8 pressure levels is hence judged satisfactory for modeling radiative processes in Saturn's atmosphere.

2.3.2. Sensitivity to band discretization

Choosing an appropriate set of bands for the spectral discretization is another important step. Selecting too large intervals may introduce significant errors when the Planck function and/or the opacity distribution vary significantly within a band. To avoid introducing too much error at this stage, one solution would be to work with many small band intervals, for instance 10-cm^{-1} wide, as chosen by Friedson and Moses (2012). However, this would imply dealing with hundreds of k-distribution tables in order to cover the whole spectral range (10–25,000 cm^{-1}), and the efficiency of computation would be lessened. We thus focus our efforts on the construction of an optimized band discretization that minimizes the number of bands without reducing the accuracy of the heating rates calculations.

Starting from a high resolution set of spectral bins, the resolution is degraded step by step, treating different spectral regions independently. For instance, in the thermal infrared, we first consider the spectral region 10–610 cm^{-1}, which is a region of strong CIA continuum and where the thermal infrared flux peaks. The bin width is degraded from 20 cm^{-1} to 100 cm^{-1} in this spectral range only, and 1-D radiative–convective runs are performed for each of the corresponding k-distribution models. Fig. 3 shows the impact of these different band discretizations on the equilibrium temperature profile. A 60-cm^{-1} wide spectral bin in this region is found to be a good compromise between the number of bins and accuracy, as it yields an error of only 0.2–0.3 K compared to the 20-cm^{-1} wide case. At the other end of the infrared spectrum, we find that the region beyond 1400 cm^{-1} does not need to be sampled with many bins: only three are needed for satisfactory accuracy. This is expected, as the Planck function at Saturn's equilibrium temperature quickly drops at these wavenumbers. In between lie the hydrocarbon emission bands contributing the most to atmospheric infrared cooling: the ν_4 methane band at 1304 cm^{-1} (7.7 µm), the ν_5 C_2H_2 band centered at 730 cm^{-1} (13.7 µm) and the ν_{12} C_2H_6 band at 822 cm^{-1} (12.2 µm). The band discretization is degraded step by step in each of these high opacity regions, and in each of the clearer regions in between. After extensive testing to achieve the highest accuracy while using the least number of bands, we retain 20 bands in total in the thermal infrared, featured in Fig. 2. The corresponding error is in the range 0.3–0.5 K, being higher at lower pressure levels.
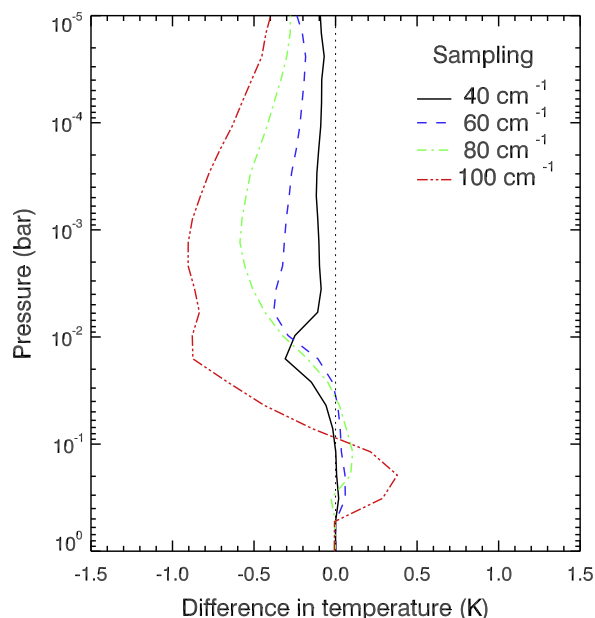

Fig. 3. Difference in temperature resulting from changing the width of the spectral bins solely in the region 10–610 cm^{-1}, from bins 20-cm^{-1} wide (reference case) to 40, 60, 80 and 100 cm^{-1} wide.

A similar methodology is used for the visible and near infrared part of the spectrum, dominated by the methane absorption bands. In this spectral region, the number of bands is reduced step by step from 59 to 17 (including 12 bands in the range 2000–7800 cm^{-1}, shown in Fig. 1), which results in an error in temperature (loss in accuracy) of 0.3–0.4 K on average. This error has a seasonal component, as it scales with the solar flux: for low insolation conditions, the error remains smaller than 0.1 K at all pressure levels, while it reaches 0.6 K at 0.01 mbar during the polar day.

2.3.3. Methane spectroscopy

Compared to its 2008 version, the HITRAN 2012 database includes major improvements regarding methane spectroscopy, both in extent and in quality: the new methane line list contains more than twice the number of lines as the 2008 compilation (Rothman et al., 2013). Of particular interest is the addition by Campargue et al. (2012) who used cavity ring down spectroscopy measurements to compile a new list in the wavenumber range from 5852 to 7912 cm^{-1}. Also, empirical lower-state energies from cold CH_4 spectra are added for the first time between 10,923 and 11,502 cm^{-1} (Fig. 1). As a consequence, using HITRAN 2012 instead of its 2008 version results in a net atmospheric heating, as methane absorption is increased in the visible/near infrared region. Quantitatively, the temperature modeled with the HITRAN 2012 line list is found to be warmer by 2 to 4 K in the range 100 to 0.01 mbar compared to using HITRAN 2008 (Fig. 4).

Despite the recent improvements in the spectroscopic databases, there are still important data gaps in the CH_4 line list in the near infrared spectral region. The absorption band at 1 µm (centered at 10,100 cm^{-1}) is still missing in HITRAN 2012, and no methane absorption coefficients are available beyond 11,502 cm^{-1} (see Fig. 1). More generally, HITRAN 2012 is known to be relatively incomplete beyond 7900 cm^{-1}. In order to complement HITRAN 2012, k-distribution coefficients are computed from Karkoschka and Tomasko (2010) methane band model in the range 5300–25,000 cm^{-1}. To do so, a method similar to the one described in Irwin et al. (1996) is used. In a first step, using Karkoschka and Tomasko (2010) tabulated band data, the
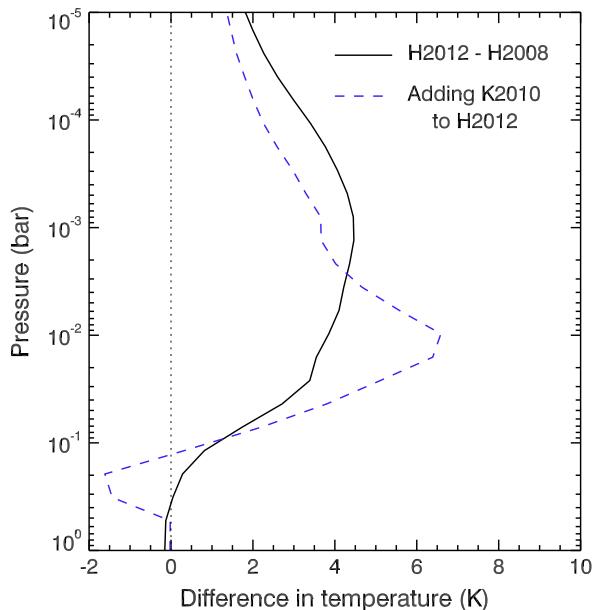
Fig. 4. Difference in temperature when using HITRAN 2012 instead of HITRAN 2008 database (solid line), and when adding Karkoschka and Tomasko (2010) methane band model to using HITRAN 2012 alone (dashed line).

atmospheric transmission $Tr(m)$ is computed at different (p, T) conditions, for different spectral bins and for 60 different methane amounts (pathlengths m), using a Goody–Voigt model. Examples of transmissions calculated as a function of pathlength are shown on Fig. 5. The transmission can also be approximated by the exponential sum:

$$Tr(m) = \sum_{1}^{N} \exp(-k_i m)\Delta g_i \qquad (1)$$

where k_i and Δg_i are the absorption coefficients and weights evaluated at the 16 abscissas i in g-space. The k-coefficients k_i for each spectral interval, temperature and pressure are then derived from an exponential sum fit to the transmissions calculated at the first step.

To validate our calculations, the coefficients obtained from our k-distribution model (using HITRAN 2012) are compared to that derived from Karkoschka and Tomasko (2010) band model in overlapping spectral bins. Fig. 6 shows such an example for the
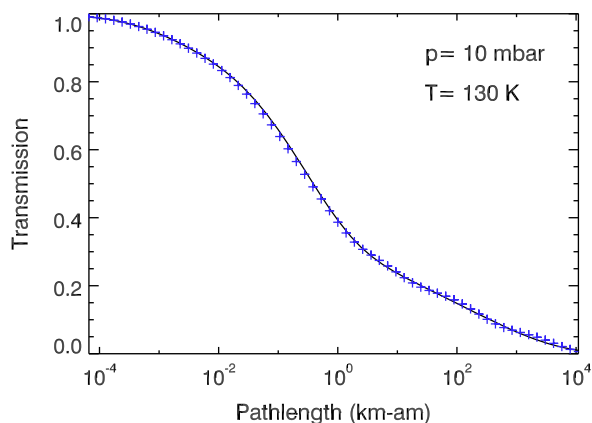

Fig. 5. Transmissions calculated from a Goody–Voigt model from the data of Karkoschka and Tomasko (2010) for the band 5900–6300 cm^{-1} (solid line) and calculated from Eq. (1) after an exponential sum fitting procedure (crosses).
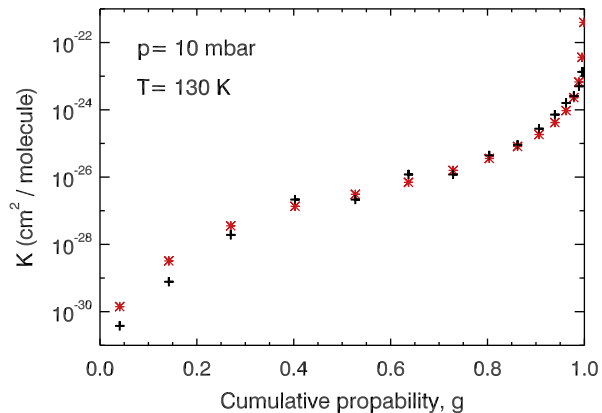

Fig. 6. k-Distribution coefficients for the band 5900–6300 cm^{-1} derived from HITRAN 2012 (red stars) and from an exponential sum fitting of the transmissions calculated from Karkoschka and Tomasko (2010) band model (crosses). (For interpretation of the references to color in this figure legend, the reader is referred to the web version of this article.)

bin 5900–6300 cm^{-1}, at a pressure of 10 mbar and a temperature of 130 K, with the corresponding fit to $Tr(m)$ shown in Fig. 5. In general, the k-distributions calculated using the two independent methods and datasets match satisfactorily in the tested range 5300–7800 cm^{-1}, and result in similar temperature profiles.

Our final $k(g)$ coefficients in the visible and near infrared part of the spectrum is a combination of 12 bins in the range 1800–7800 cm^{-1} (1.28–5.5 μm) obtained using HITRAN 2012 (see Fig. 1) and 18 bins in the range 7800–25,000 cm^{-1} (0.4–1.28 μm) using the above-described exponential sum fitting procedure. Even though the latter spectral range contains rather weak methane absorption bands compared to the strong CH$_4$ bands at 1.4, 1.7, 2.3, and 3.3 μm, using this more comprehensive spectrum of methane absorption has a significant impact on the heating rates. Fig. 4 shows that adding k-distribution coefficients derived from Karkoschka and Tomasko (2010) data increases the temperature by 3–6 K, with a maximum effect in the lower stratosphere (10 mbar). This is consistent with the fact that mean solar flux deposition occurs at greater pathlength (hence higher pressure levels) for weaker absorption bands.

2.4. Aerosols

Saturn's opaque hazes are responsible for its characteristic nebulous appearance in the visible and control the vertical distribution of solar heat deposition in the upper troposphere (Pérez-Hoyos and Sánchez-Lavega, 2006). In what follows, we report on sensitivity studies performed for different aerosol scenarios, built upon observational constraints, and study their impact on the vertical profiles of temperature and heating rates using 1-D radiative–convective runs.

2.4.1. Observational constraints

Many observational constraints on aerosol properties have been derived, mostly from Hubble Space Telescope images (Karkoschka and Tomasko, 1993; Muñoz et al., 2004; Karkoschka and Tomasko, 2005; Pérez-Hoyos et al., 2005) and more recently using the Cassini Imaging Science Subsystem (Roman et al., 2013). In those studies, the authors reproduce the observed visible and near-IR reflectivity with a model atmosphere comprising two haze layers located above a thick deep cloud. Common findings of the various models are that the upper stratospheric haze layer is optically thin (typically $\tau = 0.1$–0.2 at 600 nm, but up to 0.5 at high latitudes) and populated with small particles ($r = 0.1$–0.2 μm); while the

lower haze is located in the upper troposphere, is optically thick ($\tau = 5$–40 at 600 nm) and comprises larger particles ($r = 0.5$–3 μm). The inferred thickness and vertical extent of the upper haze vary among the different studies, as it sometimes lies between 1 and 10 mbar and other times between 10 and 100 mbar. As for the tropospheric haze, its pressure top is commonly located at tropopause level (50–120 mbar), with a base in the range 400–700 mbar. Between the two layers, some models consider an aerosol-free gap while others choose to merge the top of the tropospheric haze with the bottom of the stratospheric haze.

On top of this overall picture, complex and irregular meridional and seasonal variations in opacity, particle size and vertical distribution of the tropospheric haze have been reported. For instance, in the visible, the tropospheric haze is found optically thicker (by a factor of two) in the winter and spring hemispheres compared to the summer hemisphere, and also optically thicker at the equator compared to mid-latitudes (Pérez-Hoyos et al., 2005). In the thermal infrared (5 μm), however, a larger haze opacity is observed in the summer with respect to that in the winter hemisphere (Fletcher et al., 2011). This apparent contradiction can be partially explained by different particle sizes, as larger particles are observed in summer and autumn compared to that in winter and spring (typically 2–3 μm vs. 0.5–1 μm) (Karkoschka and Tomasko, 2005).

Another aerosol signature, although indirect, can be inferred from the tropospheric temperature profiles obtained from thermal infrared spectroscopy. Evidence for a temperature 'knee' located at 150–200 mbar has been first reported by Hanel et al. (1981) from Voyager data analysis and was later studied by Fletcher et al. (2007) from Cassini data. This signature varies seasonally, as it was seen by Voyager only in the autumn hemisphere at $L_s = 10°$ and by Cassini in the equatorial region and summer hemisphere at $L_s = 300$–$320°$. Absorption of solar photons by a tropospheric haze layer was proposed as a possible mechanism for this temperature knee.

2.4.2. Sensitivity studies

Given the range of observed aerosol scenarios, extensive sensitivity tests are performed to evaluate the impact of using different aerosol sizes, opacities and vertical distributions on the vertical profiles of temperature, the heating rates, and on the Bond albedo. Regarding the nature of these aerosols, little is known about their composition, but some observational constraints on their optical properties exist. We choose to set the real and imaginary part of the refractive index to that derived by Karkoschka and Tomasko (1993). Single scattering albedo and extinction coefficients are then calculated based on Mie theory, assuming spherical particles, based on the aerosol scheme of Madeleine et al. (2012).

In our model, the above-mentioned two-layer structure is adopted, with an optically thick layer in the upper troposphere populated with micrometer-size particles, and an optically thin stratospheric layer comprising smaller particles. Within each of these two layers, the aerosol scale height is set to the gas scale height, i.e. the aerosol optical depth varies linearly with pressure. In between, a smooth opacity profile linking the two layers is adopted, since an intermediate aerosol-free layer is found to induce too abrupt vertical gradients in the temperature profile. In practice, input parameters are the two values of the optical depth of the lower and upper hazes, their two particle sizes and four pressure boundaries. An aerosol opacity profile is constructed as described above (illustrated in Fig. 7), then the total integrated aerosol optical depth is normalized to the sum of the lower and upper hazes optical depths.

Modeling results are found to be not very sensitive to small variations of the location of the top of the stratospheric haze layer or the bottom of the tropospheric layer. These two parameters are
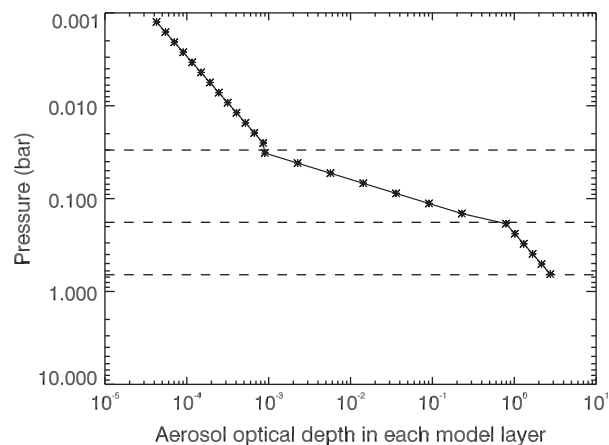

Fig. 7. Aerosol opacity profile (defined at 600 nm) as parameterized in the radiative transfer model.

thus held constant at 1 mbar and 660 mbar, respectively. Likewise, the integrated opacity of the upper haze is set to $\tau = 0.1$ (at 600 nm) and stratospheric particle sizes to $r = 0.1$ μm, corresponding to typical observed values (these parameters are not observed to vary much with latitude and seasons, except at high latitudes). Several cases are considered for the location of the top of the tropospheric layer, p_{top}: either 100 mbar (close to tropopause level, consistent with Roman et al. (2013) and Pérez-Hoyos et al. (2005) analyses) or 180 mbar (corresponding to the typical location of the temperature knee observed by Fletcher et al. (2007)). The location of the bottom of the stratospheric layer is also varied between 100 mbar and 30 mbar.

Our 1-D radiative–convective simulations show that maximum heat deposition occurs at the top of the tropospheric layer and that solar radiation does not penetrate below the 600-mbar pressure level, in agreement with Pérez-Hoyos et al. (2005). Heating by the tropospheric haze layer induces a more or less pronounced temperature knee located at the haze pressure top. Hence, in order to be consistent with the Fletcher et al. (2007) observations, the scenario with $p_{top} = 180$ mbar is retained. Besides, setting the bottom of the stratospheric haze layer at 30 mbar better reproduces the observed tropopause location ($\sim$90 mbar). Finally, we find that the upper stratospheric haze (as parameterized here) do not significantly impact the temperature field.

For this chosen vertical distribution, the sensitivity to the integrated opacity of the tropospheric haze layer, τ_{tropo} (defined at 600 nm), is studied by varying it between 5 and 30 (not shown). As can be expected, heating by aerosols is found to be commensurate with optical depth. For a given haze opacity, the temperature sensitivity to different sizes is also explored by varying the particle sizes r between 0.2 and 4 μm. Small particles are found to be less efficient in heating the atmosphere than larger particles, as can be seen in Fig. 8. This can be explained by the fact that in the visible range, smaller particles have a larger single scattering albedo, hence are less absorbing. For instance, at 600 nm, the single scattering albedo ω ranges from 0.9966 for $r = 0.5$ μm to 0.9711 for $r = 4$ μm.

The temperature sensitivity to different particle sizes is less pronounced in winter than in summer. For instance, temperature difference at 180 mbar, 20°S, between a scenario with $r = 0.4$ μm and that with $r = 3$ μm is found to be 6 K in summer (as pictured in Fig. 8) but 3 K in winter. This difference can be explained by seasonal variations in incoming insolation, hence in the available amount of solar photons to be absorbed by the haze. This effect is illustrated in Fig. 9, which compares the heating rate profiles calculated for a clear atmosphere and for a typical aerosol scenario, at
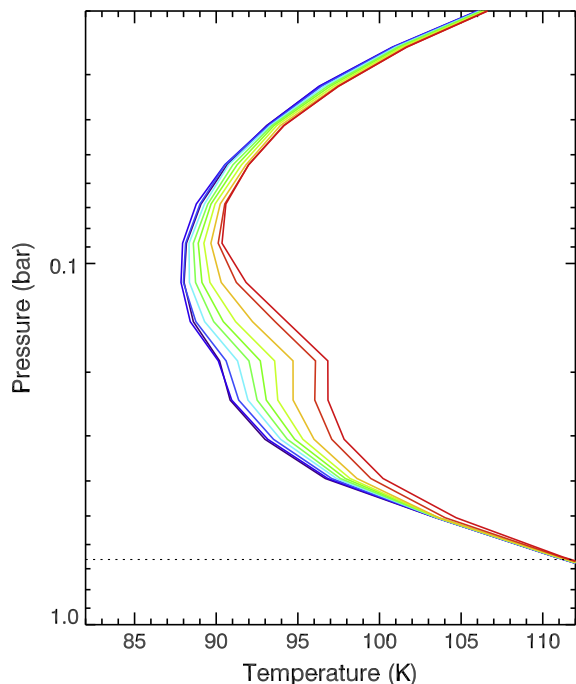
Fig. 8. Temperature profiles modeled at 20°S, $L_s = 300°$ with $\tau_{tropo} = 15$ and various tropospheric particle sizes (0.2, 0.4, 0.6, 0.8, 1, 1.2, 1.5, 2, 3 and 4 μm, from blue to red). (For interpretation of the references to color in this figure legend, the reader is referred to the web version of this article.)

two different seasons. In the case of a clear atmosphere, the atmospheric heating rate steadily decreases with increasing pressure and is very low at the 200-mbar pressure level and below. As a result, no significant temperature seasonal variations are produced in the upper troposphere. However, in the presence of aerosols, a peak in solar heating localized at the top of the haze layer is produced. This peak is greater in summer than in winter and reinforces the seasonal variations of temperature. This is in qualitative agreement with the analysis of Fletcher et al. (2007) who observed the temperature knee preferentially in the summer season.

In summary, upper tropospheric aerosols induce a significant atmospheric heating that is commensurate with the particle size,
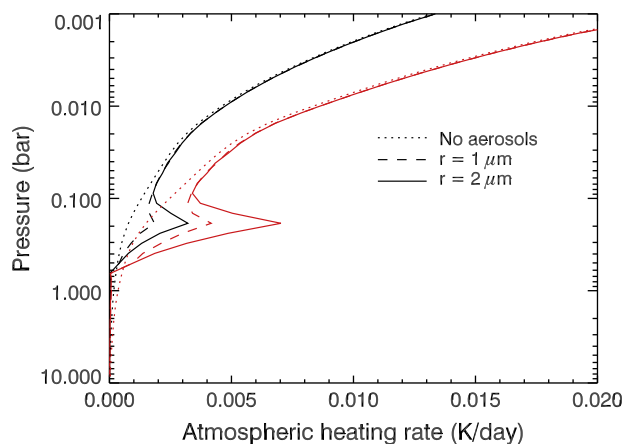

Fig. 9. Atmospheric heating rates profiles obtained with aerosols (solid and dashed lines) or for a clear atmosphere (dotted lines) at 20°S for $L_s = 120°$ (winter, in black) and $L_s = 300°$ (summer, in red). Integrated aerosol opacity is set to 15, and two different particle sizes r are used. (For interpretation of the references to color in this figure legend, the reader is referred to the web version of this article.)

the optical depth and the incoming solar flux. For a given aerosol scenario (a fixed particle size and opacity), a seasonal effect takes place without the need for invoking time-dependent aerosol properties. This behavior was already suggested by Fletcher et al. (2007) and Friedson and Moses (2012).

2.4.3. Choice of a nominal aerosol scenario

Given the results of these sensitivity studies, we then investigate if a simple aerosol scenario (uniform with latitude and season) allows to reproduce the observational constraints on the temperature knee and the Bond albedo (0.342 ± 0.03, as derived by Hanel et al. (1983)), or if a more complex scenario is needed. We find that in order to produce a temperature knee in the summer hemisphere, a value of τ_{tropo} of at least 8 and particles larger than 1 μm, are needed. Similarly, in order not to produce a knee in the winter hemisphere, τ_{tropo} must either be smaller than 10, or tropospheric particles must be smaller than 2 μm. Among this family of solutions, we choose to retain the case $\tau_{tropo} = 8$, $r_{tropo} = 2$ μm, that corresponds to a Bond albedo of 0.352, close to the measured value. The impact of using different aerosol scenarios on the latitudinal temperature structure is assessed in Section 3.3.

2.5. Radiative balance and establishment of equilibrium

Our radiative–convective model is flexible and can be run in a 1-D version (either at a given latitude or for globally-averaged conditions), or directly for the whole planet, in 3D. The 1-D version is used to perform sensitivity studies to various parameters (as detailed in previous sections), but also to study the radiative balance and how the equilibrium temperature is reached. To do this, different configurations are evaluated, running the 1-D model for globally-averaged conditions with or without aerosols, with or without an internal heat flux, and starting from different initial conditions: from a cold (100 K) or warm (150 K) isothermal profile. To evaluate the radiative balance, useful diagnostic variables are the amount of outgoing longwave radiation (OLR) compared to the absorbed solar radiation (ASR), and the value of the Bond albedo, defined as 1-ASR/ISR, where ISR is the incoming solar radiation.

We find that including an internal heat flux and aerosol layers allows the model to match not only Saturn's Bond albedo but also its total emitted power (4.93 W m^{-2} compared to the value of 4.95 W m^{-2} measured by Li et al. (2010)). Furthermore, in our simulations, radiative balance is respected, i.e. the OLR equals the ASR plus the internal heat flux to a precision of about 1.8%. Without an internal heat flux, tropospheric temperatures would be colder by 30 K and the associated emitted power would be too low (2.5 W m^{-2}). If no aerosols or cloud layers are considered, the resulting Bond albedo is too low (0.15), tropospheric temperature are too high and as a result, Saturn's emitted power is too high (5.75 W m^{-2}). Furthermore, in the absence of aerosol or cloud layers, model results are very sensitive to the choice of the bottom pressure level (3 bar or 10 bar) owing to unbalanced solar absorption and upward Rayleigh scattering of solar radiation. Including an opaque tropospheric haze layer is thus key to ensure that Saturn's radiative balance is respected.

For this nominal set-up (aerosols and internal heat flux included), stratospheric temperatures above the 10 mbar level are found to reach equilibrium after one Saturn year, regardless of the initial profile, i.e. the stratospheric temperatures at the end of the second simulation year are equal to that at the end of the first year. Below ~500 mbar, the temperature evolves much slower, as shown in Fig. 10. This behavior is expected, as this region lies below the radiative–convective boundary, where radiative exchanges are less efficient. In the first model layers, the atmosphere is heated by the internal heat flux, and heat is transported
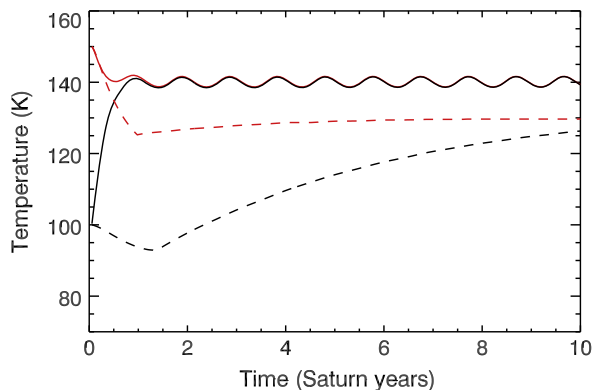
Fig. 10. Temperature at 1 mbar (solid lines) and 1 bar (dashed lines) calculated from a 1-D version of the model (globally-averaged conditions), starting from isothermal profiles at 100 K (black) or 150 K (red). (For interpretation of the references to color in this figure legend, the reader is referred to the web version of this article.)

upward through convective adjustment. In addition, as the radiative time constant scales as p/T^3, the establishment of equilibrium is strongly dependent on the initial temperature profile. Starting from a cold profile, the temperature at 1 bar can reach equilibrium only after ∼20 years, while it takes about 4 years if the model is initialized close to its equilibrium temperature value in the first model layers (see Fig. 10).

For reference, the main elements of our nominal model are summarized in Table 2.

3. Results from global radiative–convective simulations

The radiative–convective model is now run globally, at a resolution of 128 (latitude) × 64 (altitude) grid points. The longitudinal dimension is not needed here, as the diurnal cycle is neglected. However, we note that the 3D capability is already implemented in the framework of the LMD generic GCM, and will be employed in future studies coupling the dynamical core to the radiative–convective model.

To mitigate the long equilibrium timescales in the troposphere, these 2D runs are initialized with a realistic vertical temperature profile derived from a 1D simulation run that reached equilibrium. Simulations are then run for five Saturn years to ensure equilibrium, and results for the last simulation year are presented in the following sections. These results are made available in NetCDF format in Supplementary Material.

3.1. Seasonal variations

As a result of Saturn's 26.7° obliquity, significant seasonal temperature variations are produced by the 2D radiative–convective model, in particular in the stratosphere. The thermal structure at

Table 2
Summary of the nominal model.

Pressure range	$3-10^{-6}$ bar
Internal heat flux	2.6 W m^{-2}
Heat capacity	11,500 J kg^{-1} K^{-1}
Gaseous composition	H$_2$, He, CH$_4$, C$_2$H$_6$ and C$_2$H$_2$
Spectroscopic data	HITRAN 2012 + Karkoschka and Tomasko (2010) for CH$_4$ in the region 7800–25,000 cm^{-1}
Stratospheric aerosols	$\tau = 0.1$, $r = 0.1$ μm, $p_{top} = 1$ mbar, $p_{bottom} = 30$ mbar
Tropospheric aerosols	$\tau = 8$, $r = 2$ μm, $p_{top} = 180$ mbar, $p_{bottom} = 660$ mbar
Geometric effects	Ring shadowing, oblateness

the 1-mbar pressure level is shown in Fig. 11 as a function of latitude and season. At this pressure level, the temperature at the South Pole ranges from 113 K in winter to 158 K in summer. A closer look at the model outputs reveals that summer polar temperatures reach a maximum after a 30° phase lag in heliocentric longitude (Ls) following the summer solstice. In contrast, winter polar temperatures continuously cool down during the polar night and reach a minimum 90° in Ls after the winter solstice, hence at the spring equinox. The eccentricity of Saturn's orbit also impacts the temperature field: throughout the stratosphere, Southern summer temperatures are found to be ∼4 K warmer than during the Northern summer, consistently with the fact that Saturn's perihelion occurs at Ls = 280°, close to the Southern summer solstice.

Overall, at 1 mbar, a maximum pole-to-pole contrast of 40 K is obtained between the winter and summer hemispheres at Ls = 317°, *i.e.* with a phase lag of 47° in solar longitude following the solstice (Ls = 270°). This value of maximum inter-hemispheric temperature contrast decreases with increasing pressure, varying from 50 K at 0.01 mbar to 10 K at 200 mbar. In parallel, the associated phase lag increases with pressure, as the radiative timescale increases: this lag varies between 30° in Ls at the 0.01-mbar pressure level to 90° in Ls at the 200-mbar level. Below the 400-mbar pressure level, no significant seasonal or orbital temperature response is observed. Rather, the modeled temperatures exhibit a maximum at the equator and a small, symmetric decrease towards both poles, consistently with radiative timescales being longer than Saturn's year at these pressure levels.

To first order, these results agree well with existing models, for instance that of Bézard et al. (1984) and Greathouse et al. (2008), both in terms of seasonal contrast and phase lag of the temperature extrema. One noticeable difference with Greathouse et al. (2008) model is that the authors find warmer temperatures in the Northern than in the Southern summer at the 0.5-mbar pressure level, which is in apparent contradiction with the asymmetry in radiative forcing associated to Saturn's eccentricity. This may be explained by the use of different hydrocarbon meridional distributions. Our model assumes uniform hydrocarbon abundances with latitude, while Greathouse et al. (2008) set the C$_2$H$_2$ and C$_2$H$_6$ abundances to follow the meridional distributions observed by Cassini in 2005–2006, and hold them fixed with time. As these hydrocarbons are key stratospheric coolants, we expect the atmospheric cooling rates to be greater in the model of Greathouse et al. (2008) at latitudes where their C$_2$H$_2$ and C$_2$H$_6$ abundances exceed ours, as it is the case at high southern latitudes. Hence, the higher hydrocarbon abundances close to the south pole in Greathouse et al. (2008) model would explain their colder temperatures in this region. The sensitivity to different hydrocarbon abundances in our model is studied in more detail in Section 4.4.
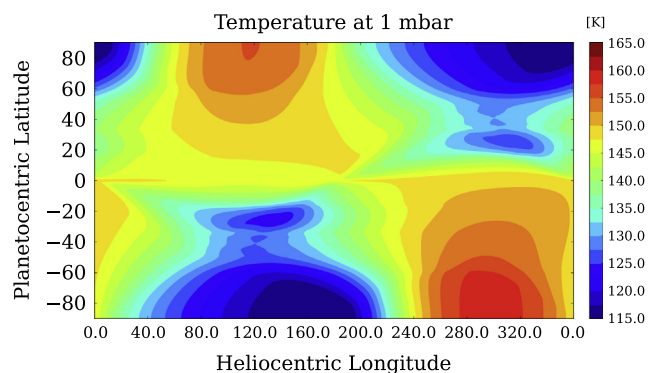

Fig. 11. Temperature map at 1 mbar with latitude and season produced by the radiative–convective model. By convention, the heliocentric longitude of 0° corresponds to the Northern spring equinox.

3.2. Impact of ring shadowing

Saturn's ring shadowing has an important impact on the stratospheric temperature field. It is responsible for the cold temperatures seen at ∼25° of latitude in the winter hemisphere in Fig. 11. Fig. 12 shows in more details the vertical and meridional structure of the cold temperature anomaly induced by the rings close to the Northern winter solstice (Ls = 300°). Ring shadowing induces a local, seasonal cooling up to 22 K in the upper stratosphere (0.01 mbar) compared to a model run performed without the rings. At the tropopause level (100 mbar), cooling by ring shadowing is at most 4 K. This signature is mostly localized in the winter hemisphere (under the ring's shadow), although a signature reminiscent of the previous season is visible in the opposite hemisphere at the 10-mbar pressure level. This is consistent with a radiative timescale on the order of half a kronian year at this pressure level. Overall, the temperature anomaly is the strongest and lasts the longest at a latitude of 20–25°. In this region, at the 1-mbar pressure level, the cold temperature anomaly remains in the range 10 K to 16 K during a full season (90° of Ls). Hence, ring shadowing represents a non-negligible component of Saturn's external radiative forcing.

3.3. Impact of different aerosol scenarios

The 2D runs presented here use a nominal aerosol scenario characterized by a tropospheric haze comprising particles of 2 μm in size and an integrated visible optical depth of 8, which corresponds to typical observed conditions in the summer hemisphere (Roman et al., 2013). The resulting temperature contrast produced by the model at the top of the tropospheric haze layer (180 mbar) between the winter and summer mid-latitudes is of 10 K, in good agreement with that observed by Fletcher et al. (2007). However, as described in Section 2.4, smaller particles have been observed during winter, associated with a larger visible optical depth. This seasonal variation of the haze properties could significantly impact the seasonal temperature contrast. An alternate 2-D radiative–convective simulation with particles of 1 μm and $\tau_{tropo} = 16$ (typical of winter conditions) is thus run to evaluate this impact. The resulting thermal structure and seasonal variations are very similar to the nominal case (differences in temperature are less that 1 K). This implies that two competing effects are canceling out: smaller particles are less efficient in heating the atmosphere, which is mitigated by a larger τ_{tropo}.

This example illustrates the degeneracy in the heating induced by aerosols: several scenarios can produce similar radiative forcings. As the primary goal of the radiative–convective model is to produce heating rates and thermal seasonal contrasts that are consistent with observ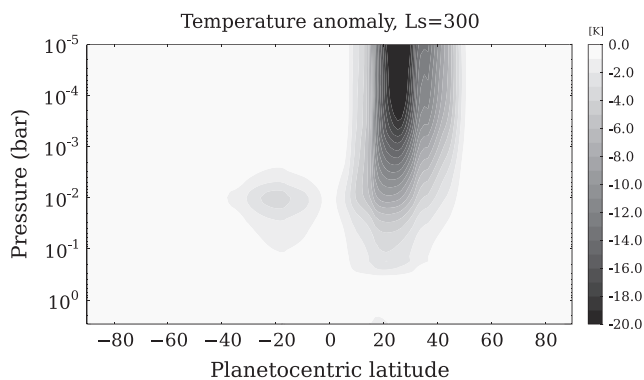ations (through effective aerosol properties), and not to reproduce in detail the observed meridional and seasonal variations of the haze properties, the nominal aerosol model is thus judged satisfactory.

3.4. Impact of Saturn's oblate shape and latitude-dependent gravity field

We investigate the impact of taking into account Saturn's oblate shape on the radiative calculations. Firstly, Saturn's oblateness of 0.098 modifies the amount of incoming solar radiation at a given planetocentric latitude compared to the spherical case. Given that our GCM uses a planetocentric grid system, this effect could have a significant impact. We find that in the oblate case, winter mid-latitudes receive up to 40% less solar radiation than in the spherical case. Consequently, stratospheric winter mid-latitude temperatures are cooler by 2 to 6 K (at the 1 and 0.01 mbar pressure levels, respectively) compared to the spherical case.

Secondly, Saturn's oblate shape and rapid rotation induces a significant meridional dependence of the gravitational field g, which varies between 8.8 (at the equator) and 12.2 (at the poles) and is also taken into account. In the radiative calculations, g plays a role in the computation of the mass of an atmospheric column, hence on opacity, which is inversely proportional to g. Consequently, we find that in the oblate, rotating case, the radiative–convective boundary (RCB) is shifted to lower pressure levels at the equator (at ∼450 mbar) and to higher pressure levels at the poles (at ∼550 mbar). This is expected, as the RCB is governed by the variation of the opacity with pressure through pressure broadening (Robinson and Catling, 2014). The opacity being smaller at the poles, solar radiation penetrate at deeper pressure levels, hence the deeper RCB. In addition, g also plays a more complex role on the heating and cooling rates, defined as

$$\frac{dT_{\odot}}{dt} = \frac{Mg}{C_p}\frac{dF_{\odot}(\tau(g))}{dP}; \quad \frac{dT_{IR}}{dt} = \frac{Mg}{C_p}\frac{dF_{IR}(\tau(g))}{dP} \quad (2)$$

which are both proportional to g (smaller at the equator in the oblate, rotating case) and to the variation of the solar ($F_{\odot}$) or infrared (F_{IR}) flux with pressure, which depends on the opacity $\tau(g)$ (larger at the equator in the oblate, rotating case). We find that taking into account the meridional dependence of g reduces the equator-to-pole contrasts of both the heating and cooling rates, by ∼10%, compared to the spherical case. Nevertheless, the two terms in Eq. (2) partly cancel out in the computation of the net heating rates. As a result, in the oblate, rotating case, the equator-to-pole temperature contrasts are only slightly reduced compared to the spherical case, by about 0.5 K in average, with a largest change in contrast of 3 K observed at the 10-mbar level.

4. Comparison to observations and discussion

4.1. Available observations

Onboard Cassini, the Composite Infrared Spectrometer (CIRS) is a Fourier transform spectrometer covering the range 10–1500 cm^{-1} (7–1000 μm). It acquires spectra of the thermal emission of the atmosphere in nadir or limb viewing geometry, allowing the retrieval of temperature profiles in the range 500–70 mbar and 5–0.5 mbar (nadir data), or between 20 and 0.005 mbar (limb measurements). Published nadir data analyses cover the period 2005–2011, roughly from pole to pole (Fletcher et al., 2007; Fletcher et al., 2010; Sinclair et al., 2013), while limb data are available mostly for the period 2005–2006 between 45°N and 80°S (Guerlet et al., 2009). Ground-based observations at high spectral resolution ($R \sim 80,000$) from the Texas Echelon Cross Echelle Spectrograph (TEXES), acquired in the Southern

Fig. 12. Temperature anomaly associated to ring shadowing at Ls = 300°.

Hemisphere in 2002, complement this dataset (Greathouse et al., 2005). Altogether, Cassini/CIRS and ground-based observations provide constraints on a large meridional, vertical and temporal range for the validation of our radiative transfer model.

4.2. Mean vertical thermal structure

The vertical thermal structure observed by Cassini/CIRS is satisfyingly reproduced by the radiative–convective transfer model, as shown in Fig. 13. Common features between the observations and the model include a qualitatively similar temperature knee at 180 mbar seen predominantly in the summer hemisphere, a tropopause located at the 100-mbar pressure level with temperatures in the range 80–90 K, and stratospheric temperatures reaching typically 140–150 K at the 1-mbar level and above. The main disagreement concerns the thermal structure in the middle to the upper stratosphere: above the 2-mbar pressure level, the modeled temperature is close to isothermal, while Cassini/CIRS and TEXES observations are consistent with a temperature increase of 15–20 K (depending on latitude) between the 2-mbar and the 0.01-mbar pressure levels. As a result, modeled temperatures are on average warmer by 5 K in the 10–0.1 mbar pressure range compared to observations, and cooler by 5 K in the 0.1–0.01 mbar pressure range (Fig. 13).

We note that the positive temperature gradient derived from Cassini/CIRS data in the upper stratosphere does not likely result from a retrieval artifact, as the retrieval method has been shown to yield consistent results (independent of the choice of the prior temperature profile) up to the ~5 μbar pressure level. Furthermore, from ground-based observations, Greathouse et al. (2005) also found a positive temperature gradient between 3 and 0.03 mbar at every observed latitude. Departures from local thermodynamic equilibrium (LTE) are unlikely responsible for producing a temperature bias in the data analysis, as the transition between LTE and non-LTE (for CH_4) is thought to occur at the ~1 μbar pressure level on Saturn (Drossart et al., 1999).

Missing radiative or dynamical processes in the model are more likely responsible for this discrepancy. Regarding the radiative processes, one can exclude the uncertainty in the vertical gradients of C_2H_6 and C_2H_2 mixing ratios as a source of error, as they are set to those retrieved from the same Cassini/CIRS observations. As for the minor species C_3H_8, CH_3C_2H, C_4H_2 and CH_3D, which radiative

effects are neglected in the model, we estimate that their combined contribution represents about 5% of the total radiative cooling rate. This implies that modeled stratospheric temperatures are probably overestimated by 1–2 K, which is not enough to account for the 5 K model-data mismatch in the middle stratosphere. Possible radiative processes left to explain this disagreement are therefore: (i) errors inherent to the spectroscopic data used to compute the absorption coefficients, and/or (ii) an unknown absorber heating the upper stratosphere. Both are challenging to assess. Dynamical processes, unaccounted for in the present model, might also play a role and will be included in future studies. In particular, the potential warming of the upper stratosphere through dissipation or breaking of inertia-gravity waves will be investigated.

4.3. Seasonal contrasts

Cassini/CIRS data acquired in 2005–2006 (Ls ~ 310°) represent an excellent opportunity to study seasonal contrasts between the summer (Southern) and winter (Northern) hemispheres, as they were acquired not long after the December, 2002 summer solstice. Figs. 14 and 15 compare the observed and modeled temperatures at the 100-mbar and 1-mbar pressure levels at this season. In the upper troposphere (300–100 mbar pressure level), the hemispheric

Fig. 14. Temperature at 100 mbar as retrieved from Cassini/CIRS nadir data (black crosses, from Fletcher et al. (2007)), at Ls = 310°, compared to modeled temperatures (red line). (For interpretation of the references to color in this figure legend, the reader is referred to the web version of this article.)
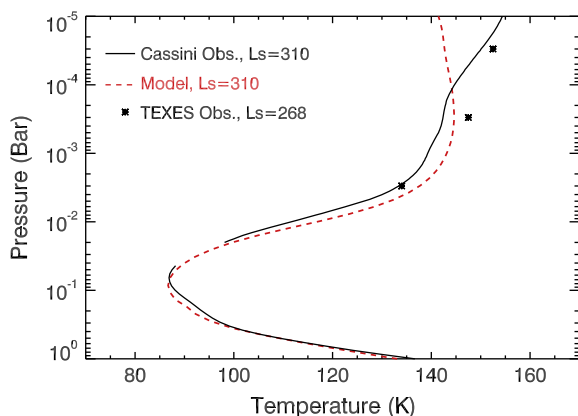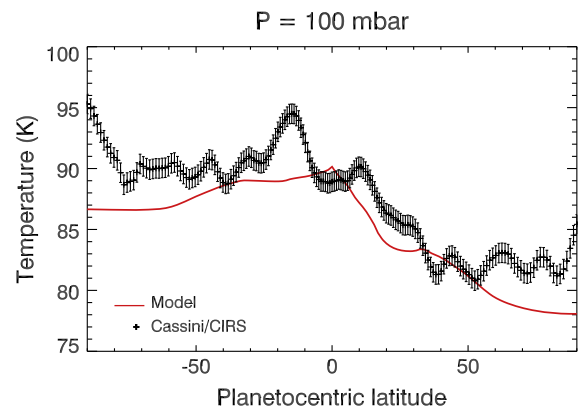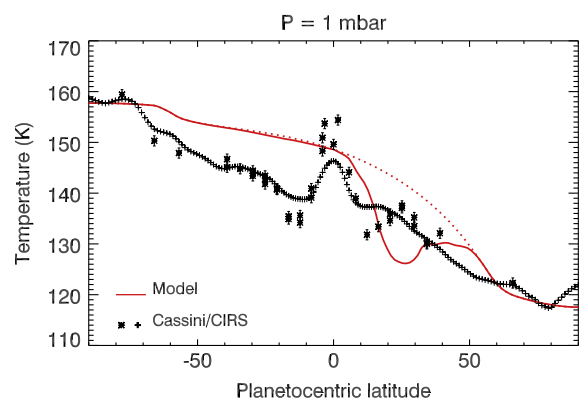

Fig. 13. Temperature profiles averaged between 40°S and 40°N as observed by Cassini/CIRS at Ls = 310° (in black, combining nadir and limb observations from Fletcher et al. (2007) and Guerlet et al. (2009)) and as produced by the model (red dashed lines). For comparison, ground-based observations acquired at 40°S, Ls = 268° are shown at three pressure levels (see also Greathouse et al. (2005)). (For interpretation of the references to color in this figure legend, the reader is referred to the web version of this article.)

Fig. 15. Temperature at 1 mbar as retrieved from Cassini/CIRS nadir (crosses) and limb (stars) measurements, at Ls = 310°, compared to modeled temperatures (red line). For comparison, a model run that neglects the ring shadowing is shown as the dotted red line. (For interpretation of the references to color in this figure legend, the reader is referred to the web version of this article.)

asymmetry observed by Fletcher et al. (2007), with temperatures 6–10 K warmer in the summer hemisphere, is well reproduced by the model. On top of this trend, small-scale temperature variations seen in the CIRS retrievals are most likely linked to the strong tropospheric jets through thermal wind balance, and hence are not predicted by our radiative–convective model.

In the stratosphere, at the 1-mbar pressure level, the observed overall meridional gradient is well reproduced by the model (Fig. 15), with temperatures in the range 120–160 K; but several model-data mismatches are noticeable. In the equatorial region, the observed temperature field is dominated by an equatorial oscillation characterized – at this pressure level and season – by a sharp local temperature maximum of 152 K at the equator, surrounded by local temperature minima of 135 K at 15°S and 132 K at 15°N. No such equatorial oscillation is produced by our radiative–convective model, which is expected as this phenomenon is thought to result from dynamical interactions between waves and the mean zonal flow (Fouchet et al., 2008; Orton et al., 2008; Guerlet et al., 2011). The warm polar hood observed by Fletcher et al. (2008), characterized by a sharp increase in temperature polewards of 70°S, is also not produced by the model. This polar warming could be caused by absorption of solar photons by specific high-latitude stratospheric aerosols, which are thought to have different optical properties (Karkoschka and Tomasko, 2005). The latter aerosols are not yet included in our model, as their vertical structure is not well constrained.

On the other hand, a striking feature in the modeled temperature field is missing from the observations: our radiative model predicts that the ring shadowing should locally decrease the temperature by ~15 K compared to surrounding latitudes, resulting in a sharp contrast of 25 K between latitudes 25°N and 25°S at the 1-mbar pressure level. In contrast, the observed temperature field features a local temperature maximum under the ring's shadow, and the temperature difference between 25°N and 25°S is only of 6 K. A dynamical origin is favored to explain this disagreement, with adiabatic cooling associated to upwelling at summer mid-latitudes and heating associated to subsidence under the ring's shadow. This scenario was already proposed by Guerlet et al. (2009, 2010) to interpret the observed asymmetries in hydrocarbon abundances and is also consistent with Friedson and Moses (2012) model results.

In addition, even though the overall meridional contrast is well reproduced at the 1-mbar pressure level, it is less the case at other pressure levels. While our radiative–convective model predicts summer-to-winter temperature contrasts that increase with decreasing pressure – consistently with shorter radiative time constants – the temperature contrast obtained from Cassini/CIRS is maximum at the 5-mbar pressure level and quickly drops with altitude. Fig. 16 points out this behavior for the entire pressure range probed by Cassini/CIRS nadir and limb measurements: at the 0.1-mbar pressure level, the temperature difference between 66°S and 40°N is less than 10 K in the observations, but predicted to be 27 K should the temperature be governed by radiative processes alone. On the other hand, below the 5-mbar pressure level, twice as high seasonal temperature contrasts are observed compared to the modeled ones. This strongly suggests that dynamical processes act to cancel out the radiatively-forced seasonal temperature contrasts in the upper stratosphere, and possibly enhance it in the lower stratosphere.

Finally, we also compare the observed seasonal changes between 2005 and 2009/2010 to our model predictions: at the 1-mbar pressure level, Fletcher et al. (2010) report a warming of the Northern mid-latitudes by 6 to 10 K as they emerge from the ring's shadows. This compares well with the 6 to 11 K warming produced by the model at similar latitudes. Regarding the Southern hemisphere, Sinclair et al. (2013) report that high latitudes should
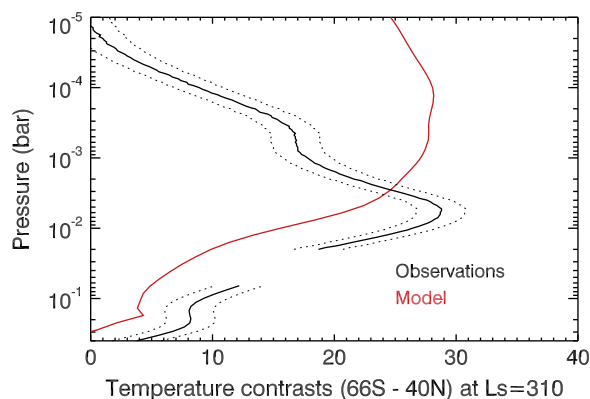

Fig. 16. Temperature contrasts, at Ls = 310, between latitudes 66°S and 40°N (planetocentric) as produced by the radiative–convective model (in red) and obtained from Cassini/CIRS measurements (in black, with error bars). (For interpretation of the references to color in this figure legend, the reader is referred to the web version of this article.)

cool down by 10 to 15 K as they evolve from mid-summer to autumn conditions, which is also in good agreement with our model, which predicts a cooling of 10–12 K. Hence, despite the several model-data mismatches that can be reported at a given date, seasonal trends observed at the 1-mbar pressure level between Ls = 300° and Ls = 10° are, to first order, well reproduced by our radiative–convective model.

4.4. Sensitivity to variations in composition

In order to investigate whether some of the above-mentioned model-data mismatches can be explained by heterogeneities in the hydrocarbon abundances, simulations were performed for various realistic hydrocarbon vertical profiles. These profiles were chosen to be representative of extreme cases measured by Cassini/CIRS: from the analysis of 2005–2006 limb data, Guerlet et al. (2009) derived high hydrocarbon mixing ratios at the equator and 25°N, and low mixing ratios in the region 20–40°S. These profiles, interpolated on the model pressure grid, are displayed and compared to the nominal case in Fig. 17. Between the two extreme cases, the hydrocarbon mixing ratios differ by a factor of two to three.

In short, we find that when using hydrocarbon profiles that better reflects the observations at latitudes 25°N and 25°S, the modeled stratospheric temperatures are about 3 K colder at 25°N in
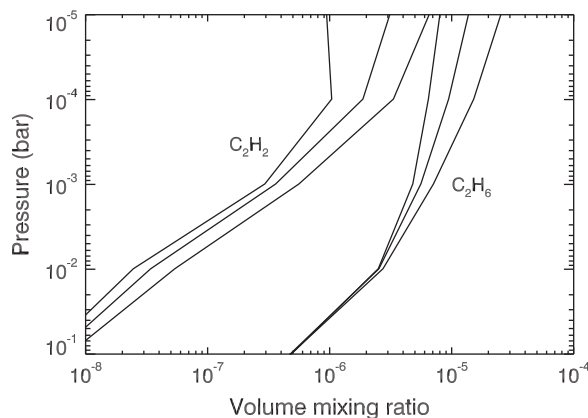

Fig. 17. Ethane (C_2H_6) and acetylene (C_2H_2) mixing ratio vertical profiles used in the model. For each species, three vertical distributions have been tested to cover the range of abundance values measured by Cassini/CIRS.

the pressure range 1–0.01 mbar (as a result of the higher cooling rates associated to more abundant hydrocarbons) and respectively 3 K warmer at 25°S. As a result, the modeled temperature contrast between the two latitudes, at 1 mbar, is increased from 24 K to 30 K at this season, which is even further from the observations. From this example, we thus conclude: (i) that the low temperature contrasts observed between summer and winter mid-latitudes cannot be explained even if more realistic hydrocarbon meridional distributions are used, and (ii) that variations in hydrocarbon abundances have a significant impact on the temperature, which advocates for the future inclusion of a photochemical scheme coupled to the global climate model.

5. A case study: application to the storm-related warm anomaly

Our seasonal, radiative model can be used to study how Saturn's atmosphere relaxes radiatively in the event of a temperature anomaly. Such a strong positive anomaly was observed in the stratosphere after the December 2010 Great White Storm, and was monitored in detail thanks to ground-based and Cassini observations. Fletcher et al. (2012) reported the observation of two warm stratospheric "beacons" in January 2011, centered at 30°N, spanning 60–80° in longitude. They were characterized by peak temperatures of 190 K at 0.5 mbar (*i.e.* 50 K warmer than the typical 140 K observed in quiescent conditions) and were both drifting westward at different speeds. The two beacons merged in late April/beginning of May 2011 to form a single one centered at 40°N, even warmer (220 K at 2 mbar). A rapid temperature drop was then observed (196.5 K measured on July 8th), followed by a slow decline of the temperature, that reaches 186 K in March 2012 (Fletcher et al., 2012).

The origin of the beacons, their merging and warming mechanisms are clearly linked to the tropospheric storm, hence dynamical in origin, and lie outside the range of application of our radiative–convective seasonal model. However, whether the temperature decrease that followed can be explained by radiative processes alone is a question that can be addressed here. To this end, a standard 1-D simulation at 40°N is first run, from which the temperature profile at $L_S = 20°$ (corresponding to May 2011) is extracted, after equilibrium is reached. This profile is then modified to feature a maximum of 220 K at 2 mbar similar to the one observed in May 2011. Then, the model is initialized at $L_S = 20°$ with this "storm" profile and a second simulation is run. The temporal evolution of the temperature at the 2-mbar pressure level is compared to the quiescent seasonal variations in Fig. 18. The 1D simulation run reproduces well the initial temperature drop: the model stratosphere cools down by 20 K in the first two months, in overall agreement with the observations (−24 K over that period). In the simulation, the temperature then decreases at a slowly rate (−10 K over the next two months, then −6 K, etc.). This is in qualitative agreement with the observed trend, however, the observed temperature is systematically 10–12 K warmer than the model after $L_S \sim 25°$. This suggests that the initial rapid cooling of the beacon in May–June 2011 could be explained by radiative processes alone, but that other processes must control the subsequent cooling rate of the warm beacon.

It is worthy of notice that the tropospheric storm underwent a major dynamical change after June, 2011 when the storm's head collided with its tail. After the collision, the storm's convective activity displayed a major decline, although several weaker resurgences have been observed in August, September and December, 2011 (Sayanagi et al., 2013). As the initial warming phase of the beacon (in January–May 2011) seems to be correlated with an intense tropospheric storm activity, it is then possible that weak resurgences may have also warmed the stratosphere sporadically.
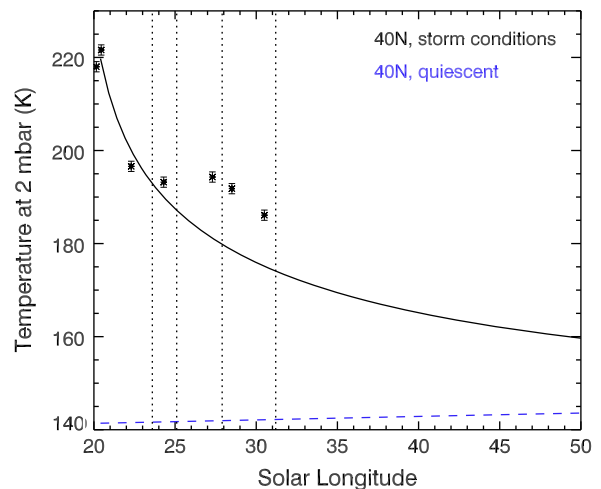

Fig. 18. Evolution of the stratospheric temperature at 2 mbar, 40°N, from a 1D radiative simulation initialized with a warm, storm-like profile (solid line) compared to quiescent conditions (blue dashed line). Stars indicate temperature measurements from thermal infrared spectra obtained by Fletcher et al. (2012) between May 2011 and March 2012. Vertical dashed lines indicate when weak resurgences of the storm were observed. (For interpretation of the references to color in this figure legend, the reader is referred to the web version of this article.)

This would explain why the observed temperatures do not follow the purely radiative cooling trend calculated with our 1D model, but remain warmer.

Finally, our simulation suggests that the warm anomaly would remain visible until at least $L_S \sim 80°$ (2016), should it be governed by radiative processes only. Further comparison with Cassini/CIRS data acquired since 2012, along with simulations with different hydrocarbon distributions, will help better constrain the beacon evolution and its mechanism in future studies.

6. Conclusion

A generic radiative–convective model developed at LMD has been adapted for Saturn's atmosphere: its composition, aerosol properties, internal heat flux, ring shadowing and oblateness have been accounted for and their impact evaluated through sensitivity studies. Furthermore, several aspects of the radiative transfer calculations have been optimized (use of up-to-date spectroscopic data, tailored band discretization).

To first order, the resulting vertical thermal structure and seasonal contrasts agree well with those retrieved from Cassini/CIRS data. However, we report several important model-observation mismatches:

- The modeled temperature profile is close to isothermal above the 2-mbar level, while the temperature retrieved from ground-based or Cassini/CIRS continues to increase with altitude.
- Observed seasonal contrasts between the summer and winter hemispheres decay with height above the 5-mbar pressure level, while the radiative–convective model predicts that seasonal contrasts should remain large (~25–28 K at Ls = 300°) throughout the middle and upper stratosphere.
- A local temperature minimum associated to the ring shadowing is expected from the model (temperature 10 K cooler at the 1-mbar pressure level and 25°N), while a local temperature maximum is observed in this region.

It is unlikely that our model is missing key elements in the computation of the heating/cooling rates, except for specific polar aerosols, and unless unknown key absorbers are missing. Hence,
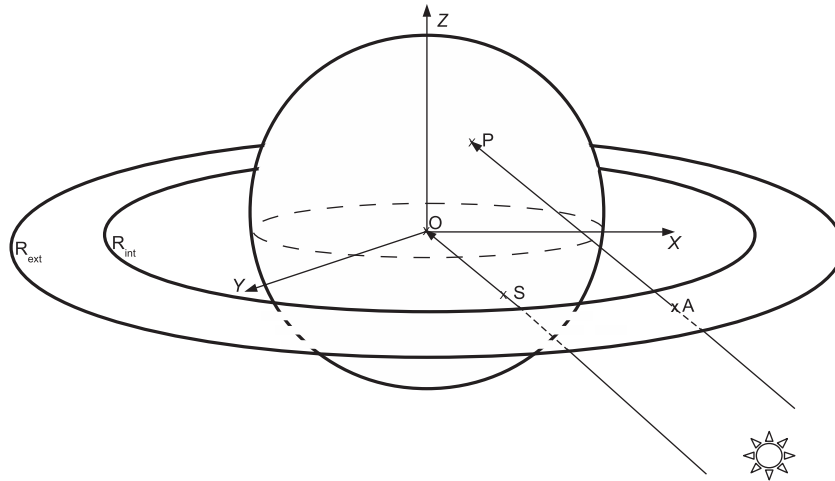
Fig. B.19. Schematic view of the ring shadowing geometry.

the observed departures from the calculated radiative–convective equilibrium are most probably driven by dynamical processes (waves, advection, eddies) and will be addressed in more details using our General Circulation Model of Saturn's stratosphere, currently being developed. Future Cassini/CIRS and ground-based observations of seasonal variations in temperature and composition will also be extremely valuable to better understand which processes control Saturn's stratospheric temperatures, chemistry and dynamics.

Finally, we illustrate that the radiative–convective model can be used to study the evolution of temperature anomalies such as the stratospheric beacon associated to the 2010 Great White Spot. Comparison with Cassini/CIRS observations performed in 2010–2011 suggests that the first rapid cooling phase of the beacon could be explained by radiative processes alone. Observations on a longer timeline are now needed to better characterize and constrain the mechanisms governing the long-term evolution of the "beacon".

Acknowledgments

Appendix A. Calculation of the ring shadowing geometry

To determine Saturn's ring shadowing effect on the incoming solar flux, the main method published in the literature proposes to find between which longitudes and latitudes the shadow of the rings is projected (Bézard, 1986; Brinkman and McGregor, 1979). Since in a GCM each grid mesh is treated individually by the radiative transfer module, it appears more straightforward to check, for each point P of the model grid, under which rings' shadow it is located (if any).

Should O be the center of the planet and A the intersection between the incoming solar ray and the equatorial plane, P is under the shadow of a ring of internal radius R_{int} and external radius R_{ext} if $R_{int} \leqslant OA \leqslant R_{ext}$ (cf. Fig. B.19). The distance OA is calculated by considering that the two Sun rays $\overrightarrow{PA}$ and $\overrightarrow{OS}$, where S is the subsolar point, are colinear. This yields

$$OA = \sqrt{\left(x - \frac{z}{z_s}x_s\right)^2 + \left(y - \frac{z}{z_s}y_s\right)^2}$$

Table B.3
Internal and external radius of the rings (in units of Saturn's equatorial radius) and corresponding normal opacities.

R_{int}	R_{ext}	τ
C ring		
1.24	1.29	0.06
1.29	1.43	0.10
1.43	1.53	0.14
B ring		
1.53	1.64	1.29
1.64	1.83	5.13
1.83	1.95	2.84
Cassini division		
1.95	1.99	0.06
1.99	2.03	0.24
A ring		
2.03	2.06	1.24
2.06	2.09	0.81
2.09	2.12	0.67
2.12	2.27	0.58

where (x, y, z) and (x_s, y_s, z_s) are Cartesian coordinates for respectively P and S. Additional conditions on P being under a ring's shadow are that P is in the winter hemisphere ($\theta \times \theta_s < 0$ where θ and θ_s are planetocentric latitudes for respectively P and S) and in the daylight ($\overrightarrow{OP} \cdot \overrightarrow{OS} \geqslant 0$).

If a point P is under a ring shadow, the incoming solar flux is reduced accordingly given the ring opacity. Opacities from the A, B and C rings (and from the Cassini division) are accounted for with values obtained through Cassini/UVIS occultations (Colwell et al., 2010) and reproduced in Table (B.3). The influence of Saturn diurnal cycle on radiative heating rates is negligible, hence our GCM employs daily averages of incoming sunlight in which ring shadowing is accounted for through the described method.

Appendix B. Supplementary material

Supplementary data associated with this article can be found, in the online version, at http://dx.doi.org/10.1016/j.icarus.2014.05.010.

References

Appleby, J.F., Hogan, J.S., 1984. Radiative–convective equilibrium models of Jupiter and Saturn. Icarus 59, 336–366. http://dx.doi.org/10.1016/0019-1035(84)90106-4.

Baldwin, M.P. et al., 2001. The quasi-biennial oscillation. Rev. Geophys. 39, 179–229. http://dx.doi.org/10.1029/1999RG000073.

Bézard, B., 1986. Variations Saisonniere de la Structure Thermique et Composition Chimique de Jupiter, Saturn, et Uranus. Ph.D. Thesis, Univ. Paris 7, Paris, France.

Bézard, B., Gautier, D., 1985. A seasonal climate model of the atmospheres of the giant planets at the Voyager encounter time. I – Saturn's stratosphere. Icarus 61, 296–310. http://dx.doi.org/10.1016/0019-10358590110-1.

Bézard, B., Gautier, D., Conrath, B., 1984. A seasonal model of the saturnian upper troposphere comparison with Voyager infrared measurements. Icarus 60, 274–288. http://dx.doi.org/10.1016/0019-1035(84)90189-1.

Brinkman, A.W., McGregor, J., 1979. The effect of the ring system of the solar radiation reaching the top of Saturn's atmosphere – Direct radiation. Icarus 38, 479–482. http://dx.doi.org/10.1016/0019-1035(79)90202-1.

Campargue, A., Wang, L., Mondelain, D., Kassi, S., Bézard, B., Lellouch, E., Coustenis, A., Bergh, C.d., Hirtzig, M., Drossart, P., 2012. An empirical line list for methane in the 1.26–1.71 μm region for planetary investigations (T = 80-300 K). Application to Titan. Icarus 219, 110–128. http://dx.doi.org/10.1016/j.icarus.2012.02.015.

Charnay, B. et al., 2013. Exploring the faint young Sun problem and the possible climates of the Archean Earth with a 3-D GCM. J. Geophys. Res. 118, 10414. http://dx.doi.org/10.1002/jgrd.50808.

Colwell, J.E., Esposito, L.W., Pettis, D., Sremčević, M., Jerousek, R.G., Bradley, E.T., 2010. Cassini Orbiter Saturn UVIS Ring Stellar Occultations 1.0. NASA Planetary Data System, CO-SR-UVIS-2/4-OCC-V1.0.

Conrath, B.J., Gautier, D., 2000. Saturn helium abundance: A reanalysis of Voyager measurements. Icarus 144, 124–134. http://dx.doi.org/10.1006/icar.1999.6265.

Drossart, P., et al., 1999. Fluorescence in the 3 μm bands of methane on Jupiter and Saturn from ISO/SWS observations. In: Cox, P., Kessler, M. (Eds.), The Universe as Seen by ISO, vol. 427. ESA Special Publication, p. 169.

Flasar, F.M. et al., 2005. Temperatures, winds, and composition in the saturnian system. Science 307, 1247–1251. http://dx.doi.org/10.1126/science.1105806.

Fletcher, L.N., Irwin, P.G.J., Teanby, N.A., Orton, G.S., Parrish, P.D., de Kok, R., Howett, C., Calcutt, S.B., Bowles, N., Taylor, F.W., 2007. Characterising Saturn's vertical temperature structure from Cassini/CIRS. Icarus 189, 457–478. http://dx.doi.org/10.1016/j.icarus.2007.02.006.

Fletcher, L.N. et al., 2008. Temperature and composition of Saturn's polar hot spots and hexagon. Science 319, 79–81. http://dx.doi.org/10.1126/science.1149514.

Fletcher, L.N., Achterberg, R.K., Greathouse, T.K., Orton, G.S., Conrath, B.J., Simon-Miller, A.A., Teanby, N., Guerlet, S., Irwin, P.G.J., Flasar, F.M., 2010. Seasonal change on Saturn from Cassini/CIRS observations, 2004–2009. Icarus 208, 337–352. http://dx.doi.org/10.1016/j.icarus.2010.01.022.

Fletcher, L.N. et al., 2011. Saturn's tropospheric composition and clouds from Cassini/VIMS 4.6–5.1 μm nightside spectroscopy. Icarus 214, 510–533. http://dx.doi.org/10.1016/j.icarus.2011.06.006.

Fletcher, L.N., Hesman, B.E., Achterberg, R.K., Irwin, P.G.J., Bjoraker, G., Gorius, N., Hurley, J., Sinclair, J., Orton, G.S., Legarreta, J., García-Melendo, E., Sánchez-Lavega, A., Read, P.L., Simon-Miller, A.A., Flasar, F.M., 2012. The origin and evolution of Saturn's 2011–2012 stratospheric vortex. Icarus 221, 560–586. http://dx.doi.org/10.1016/j.icarus.2012.08.024.

Forget, F., Wordsworth, R., Millour, E., Madeleine, J.-B., Kerber, L., Leconte, J., Marcq, E., Haberle, R.M., 2013. 3D modelling of the early martian climate under a denser CO_2 atmosphere: Temperatures and CO_2 ice clouds. Icarus 222, 81–99. http://dx.doi.org/10.1016/j.icarus.2012.10.019.

Fouchet, T., Guerlet, S., Strobel, D.F., Simon-Miller, A.A., Bézard, B., Flasar, F.M., 2008. An equatorial oscillation in Saturn's middle atmosphere. Nature 453, 200–202. http://dx.doi.org/10.1038/nature06912.

Friedson, A.J., Moses, J.I., 2012. General circulation and transport in Saturn's upper troposphere and stratosphere. Icarus 218, 861–875. http://dx.doi.org/10.1016/j.icarus.2012.02.004.

Goody, R.M., Yung, Y.L., 1989. Atmospheric Radiation: Theoretical Basis. Oxford University Press.

Greathouse, T.K., Lacy, J.H., Bézard, B., Moses, J.I., Griffith, C.A., Richter, M.J., 2005. Meridional variations of temperature, C_2H_2 and C_2H_6 abundances in Saturn's stratosphere at southern summer solstice. Icarus 177, 18–31. http://dx.doi.org/10.1016/j.icarus.2005.02.016.

Greathouse, T.K., Strong, S.B., Moses, J.I., Dowling, T.E., 2008. A radiative seasonal climate model applied to Saturn. In: AAS/Division for Planetary Sciences Meeting Abstracts #40, Bulletin of the American Astronomical Society, vol. 40, p. 472.

Guerlet, S., Fouchet, T., Bézard, B., Simon-Miller, A.A., Michael Flasar, F., 2009. Vertical and meridional distribution of ethane acetylene, and propane in Saturn's stratosphere from CIRS/Cassini limb observations. Icarus 203, 214–232. http://dx.doi.org/10.1016/j.icarus.2009.04.002.

Guerlet, S. et al., 2010. Meridional distribution of CH_3C_2H and C_4H_2 in Saturn's stratosphere from CIRS/Cassini limb and nadir observations. Icarus 209, 682–695. http://dx.doi.org/10.1016/j.icarus.2010.03.033.

Guerlet, S., Fouchet, T., Bézard, B., Flasar, F.M., Simon-Miller, A.A., 2011. Evolution of the equatorial oscillation in Saturn's stratosphere between 2005 and 2010 from Cassini/CIRS limb data analysis. Geophys. Res. Lett. 38, L09201, http://dx.doi.org/10.1029/2011GL047192.

Halsey, G.W., Hillman, J.J., Nadler, S., Jennings, D.E., 1988. Temperature dependence of the hydrogen-broadening coefficient for the nu 9 fundamental of ethane. J. Quant. Spectrosc. Radiat. Trans. 39, 429–434. http://dx.doi.org/10.1016/0022-4073(88)90087-8.

Hanel, R. et al., 1981. Infrared observations of the saturnian system from Voyager 1. Science 212, 192–200. http://dx.doi.org/10.1126/science.212.4491.192.

Hanel, R.A., Conrath, B.J., Kunde, V.G., Pearl, J.C., Pirraglia, J.A., 1983. Albedo, internal heat, flux and energy balance of Saturn. Icarus 53, 262–285. http://dx.doi.org/10.1016/0019-1035(83)90147-1.

Hansen, J.E., Travis, L.D., 1974. Light scattering in planetary atmospheres. Space Sci. Rev. 16, 527–610. http://dx.doi.org/10.1007/BF00168069.

Hourdin, F., Le van, P., Forget, F., Talagrand, O., 1993. Meteorological variability and the annual surface pressure cycle on Mars. J. Atmos. Sci. 50, 3625–3640. http://dx.doi.org/10.1175/1520-0469(1993)050<3625:MVATAS>2.0.CO;2.

Irwin, P.G.J., Calcutt, S.B., Taylor, F.W., Weir, A.L., 1996. Calculated k distribution coefficients for hydrogen- and self-broadened methane in the range 2000–9500 cm^{-1} from exponential sum fitting to band-modelled spectra. J. Geophys. Res. 101, 26137–26154. http://dx.doi.org/10.1029/96JE02707.

Karkoschka, E., Tomasko, M.G., 1993. Saturn's upper atmospheric hazes observed by the Hubble Space Telescope. Icarus 106, 428–441. http://dx.doi.org/10.1006/icar.1993.1183.

Karkoschka, E., Tomasko, M., 2005. Saturn's vertical and latitudinal cloud structure 1991–2004 from HST imaging in 30 filters. Icarus 179, 195–221. http://dx.doi.org/10.1016/j.icarus.2005.05.016.

Karkoschka, E., Tomasko, M.G., 2010. Methane absorption coefficients for the jovian planets from laboratory, Huygens, and HST data. Icarus 205, 674–694. http://dx.doi.org/10.1016/j.icarus.2009.07.044.

Leconte, J. et al., 2013a. 3D climate modeling of close-in land planets: Circulation patterns, climate moist bistability, and habitability. Astron. Astrophys. 554, A69, http://dx.doi.org/10.1051/0004-6361/201321042.

Leconte, J., Forget, F., Charnay, B., Wordsworth, R., Pottier, A., 2013b. Increased insolation threshold for runaway greenhouse processes on Earth-like planets. Nature 504, 268–271. http://dx.doi.org/10.1038/nature12827.

Lian, Y., Showman, A.P., 2010. Generation of equatorial jets by large-scale latent heating on the giant planets. Icarus 207, 373–393. http://dx.doi.org/10.1016/j.icarus.2009.10.006.

Li, L. et al., 2010. Saturn's emitted power. J. Geophys. Res. 115, E11002, http://dx.doi.org/10.1029/2010JE003631.

Liu, J., Schneider, T., 2010. Mechanisms of jet formation on the giant planets. J. Atmos. Sci. 67, 3652–3672. http://dx.doi.org/10.1175/2010JAS3492.1.

Madeleine, J.-B., Forget, F., Millour, E., Navarro, T., Spiga, A., 2012. The influence of radiatively active water ice clouds on the martian climate. Geophys. Res. Lett. 39, L23202, http://dx.doi.org/10.1029/2012GL053564.

Margolis, J.S., 1993. Measurement of hydrogen-broadened methane lines in the v_4 band at 296 and 200 K. J. Quant. Spectrosc. Radiat. Trans. 50, 431–441. http://dx.doi.org/10.1016/0022-4073(93)90073-Q.

Morales-Juberias, R., Sánchez-Lavega, A., Dowling, T.E., 2003. EPIC simulations of the merger of Jupiter's White Ovals BE and FA: Altitude-dependent behavior. Icarus 166, 63–74. http://dx.doi.org/10.1016/j.icarus.2003.08.009.

Moses, J.I., Bézard, B., Lellouch, E., Gladstone, G.R., Feuchtgruber, H., Allen, M., 2000. Photochemistry of Saturn's atmosphere. I. Hydrocarbon chemistry and comparisons with ISO observations. Icarus 143, 244–298. http://dx.doi.org/10.1006/icar.1999.6270.

Muñoz, O., Moreno, F., Molina, A., Grodent, D., Gérard, J.C., Dols, V., 2004. Study of the vertical structure of Saturn's atmosphere using HST/WFPC2 images. Icarus 169, 413–428. http://dx.doi.org/10.1016/j.icarus.2003.12.018.

Orton, G.S. et al., 2008. Semi-annual oscillations in Saturn's low-latitude stratospheric temperatures. Nature 453, 196–199. http://dx.doi.org/10.1038/nature06897.

Pérez-Hoyos, S., Sánchez-Lavega, A., 2006. Solar flux in Saturn's atmosphere: Penetration and heating rates in the aerosol and cloud layers. Icarus 180, 368–378. http://dx.doi.org/10.1016/j.icarus.2005.10.009.

Pérez-Hoyos, S., Sánchez-Lavega, A., French, R.G., Rojas, J.F., 2005. Saturn's cloud structure and temporal evolution from ten years of Hubble Space Telescope images (1994–2003). Icarus 176, 155–174. http://dx.doi.org/10.1016/j.icarus.2005.01.014.

Robinson, T.D., Catling, D.C., 2014. Common 0.1 bar tropopause in thick atmospheres set by pressure-dependent infrared transparency. Nat. Geosci. 7, 12–15. http://dx.doi.org/10.1038/ngeo2020.

Roman, M.T., Banfield, D., Gierasch, P.J., 2013. Saturn's cloud structure inferred from Cassini ISS. Icarus 225, 93–110. http://dx.doi.org/10.1016/j.icarus.2013.03.015.

Rothman, L.S. et al., 2013. The HITRAN2012 molecular spectroscopic database. J. Quant. Spectrosc. Radiat. Trans. 130, 4–50. http://dx.doi.org/10.1016/j.jqsrt.2013.07.002.

Sayanagi, K.M., Dyudina, U.A., Ewald, S.P., Fischer, G., Ingersoll, A.P., Kurth, W.S., Muro, G.D., Porco, C.C., West, R.A., 2013. Dynamics of Saturn's great storm of 2010–2011 from Cassini ISS and RPWS. Icarus 223, 460–478. http://dx.doi.org/10.1016/j.icarus.2012.12.013.

Schinder, P.J. et al., 2011. Saturn's equatorial oscillation: Evidence of descending thermal structure from Cassini radio occultations. Geophys. Res. Lett. 38, L08205. http://dx.doi.org/10.1029/2011GL047191.

Sinclair, J.A., Irwin, P.G.J., Fletcher, L.N., Moses, J.I., Greathouse, T.K., Friedson, A.J., Hesman, B., Hurley, J., Merlet, C., 2013. Seasonal variations of temperature, acetylene and ethane in Saturn's atmosphere from 2005 to 2010, as observed by Cassini-CIRS. Icarus 225, 257–271. http://dx.doi.org/10.1016/j.icarus.2013.03.011.

Toon, O.B., McKay, C.P., Ackerman, T.P., Santhanam, K., 1989. Rapid calculation of radiative heating rates and photodissociation rates in inhomogeneous multiple

scattering atmospheres. J. Geophys. Res. 94, 16287–16301. http://dx.doi.org/10.1029/JD094iD13p16287.

Wordsworth, R., Forget, F., Eymet, V., 2010a. Infrared collision-induced and far-line absorption in dense CO_2 atmospheres. Icarus 210, 992–997. http://dx.doi.org/10.1016/j.icarus.2010.06.010.

Wordsworth, R.D., Forget, F., Selsis, F., Madeleine, J.-B., Millour, E., Eymet, V., 2010b. Is Gliese 581d habitable? Some constraints from radiative–convective climate modeling. Astron. Astrophys. 522, A22. http://dx.doi.org/10.1051/0004-6361/201015053.

Wordsworth, R.D., Forget, F., Selsis, F., Millour, E., Charnay, B., Madeleine, J.-B., 2011. Gliese 581d is the first discovered terrestrial-mass exoplanet in the habitable zone. Astrophys. J. 733, L48. http://dx.doi.org/10.1088/2041-8205/733/2/L48.